# Airborne Doppler Lidar Wind Field Measurements of Waves in the Lee of Mount Shasta

WILLIAM BLUMEN AND JOHN E. HART

*Department of Astrophysical, Planetary and Atmospheric Sciences, University of Colorado, Boulder, Colorado*

(Manuscript received 22 July 1987, in final form 23 November 1987)

ABSTRACT

Airborne Doppler lidar wind measurements were obtained in the lee of Mount Shasta in northern California on 28 August 1984. These data consist of line of sight wind vectors at flight level (3000 m) and along planes tilted at 1, 2 and 3 degrees below the 3000 m level. The observed field is confined to a rectangular box, encompassing the mountain, that extends about 40 km downwind and about 20 km crosswind. The spatial resolution of the measured wind field is approximately 330 m.

The upstream southwesterly flow tended to circumvent the mountain although some air did rise over the peak (at 4317 m) to initiate three-dimensional internal gravity waves in the lee. These waves are delineated in the two-dimensional divergence field $D$, determined from the downwind and crosswind velocity components on each of the tilted planes with line of sight wind vector measurements. The observed field of $D$ exhibits a peak in its power spectrum, determined along the downstream direction, at a wavelength of about 8 km with a secondary peak at about 17 km. Data from upper air soundings at Medford, Oregon and from onboard sensors establish that the 8 km wavelength represents the free wave response, which is determined by the airstream characteristics. Comparison with the power spectrum of the mountain slope indicates that the longer wavelength is a forced response.

Qualitative aspects of the lee-wave pattern are reproduced in a linear model with uniform airstream characteristics. However, the amplitude of the free wave response is underestimated by a factor of two, and the forced wave amplitude is about three times that of the free wave. In addition, the wave disturbance produced by the linear model decays more rapidly in the downstream direction than the observed wave. These discrepancies are interpreted in relation to physical features that are not contained in the linear model.

## 1. Introduction

Three-dimensional internal gravity waves have been observed in the lee of many isolated orographic features. Examples include wave motions in the lee sides of Elk Mountain in Wyoming (Clark and Gall 1982), the Olympic Mountains of Washington (Walter and Overland 1982), the Rock of Gibraltar (Cook and Coulson 1977/78) and Martian volcanoes (Pickersgill and Hunt 1981).

Laboratory models of stratified flow past three-dimensional obstacles have been carried out, for example, by Brighton (1978) and Baines (1979). Experiments are designed to focus attention on low Froude number flows: relatively large static stability and/or obstacle height. In this regime, an upstream current does not typically flow completely over the barrier. There is a tendency for fluid to flow around the obstacle in two-dimensional horizontal planes up to a certain height that is below the level of the peak. Above the layer where the characteristic horizontal bifurcation of the flow occurs, fluid does tend to flow over the peak in two-dimensional vertical planes. Brighton's experiments showed that motion in the lee may be quite complex, exhibiting variously shaped eddies, shed vortices and separation.

Atmospheric observations have not been sufficiently dense to exhibit the type of structure displayed in the laboratory analogs, although cloud patterns and aircraft measurements have established the existence of three-dimensional lee-waves which tend to predominate above the mountain peak. Theoretical work has, for the most part, been restricted to linear lee-wave models in which all the fluid moves over shallow topography in two-dimensional vertical planes, e.g., Wurtele (1957) and Crapper (1959). However, more recently, nonlinear numerical model simulations have exhibited relatively large-amplitude lee-wave responses, roll patterns in the lee and low-level bifurcation of the incident flow around the obstacle, e.g., Clark and Gall (1982) and Peltier and Clark (1983).

Doppler lidar wind measuring systems can now provide the type of spatial resolution in the wind field that is required for detailed comparisons with laboratory and numerical model experiments. Descriptions of NASA's airborne Doppler lidar system (ADLS), installed on the NASA/Ames Convair 990, *Galileo II*, have been provided by Bilbro et al. (1984), McCaul et al. (1986) and Bluestein et al. (1986). The principal characteristics of this two-dimensional wind field mea-

*Corresponding author address:* Dr. William Blumen, Center for Atmospheric Theory and Analysis, University of Colorado, Campus Box 391, Boulder, CO 80309-0391.

surement system that are applicable to the present study, are as follows. 1) Pulsed lidar emission occurs at a wavelength of 10.6 $\mu$m and the return signal, caused by atmospheric aerosol scattering, is processed digitally to obtain Doppler shifts. 2) Line of sight vector winds are provided by scanning from the side of the aircraft, in 20 degree increments fore and aft of the normal to the flight track. 3) The spatial resolution of the wind field is approximately 330 m and the range of useful information can be as great as 30 km along the line of sight depending on atmospheric aerosol content. 4) There appears to be some uncertainty in the relative errors in the wind field vectors, so that the usefulness of these data is, at the present time, primarily contained in the patterns of the flow that are depicted.

The Doppler lidar wind data presented in this study were obtained along one leg of a race track traverse around Mount Shasta, in northern California, at approximately 1700 UTC 28 August 1984. This impressive isolated orographic feature is displayed in Fig. 1. The prevailing synoptic situation is presented in section 2. The flight track and some environmental parameters appear in section 3. Two-dimensional wind vectors and two-dimensional divergence fields are displayed in section 4, and linear model calculations are compared with the analyzed divergence fields in section 5.

The principal aims of this study are 1) to establish the value and limitations of these wind data for the study of orographic flows and 2) to evaluate the relative usefulness of a linear model in the analyses of the observed fields of motion. The present investigation is necessarily preliminary since the database is very limited, there being no direct information on the vertical structure of the flow, particularly at low levels well below the mountain peak. Further, the limited data available indicates that comparison with a nonlinear model simulation would be more appropriate, although the linear model does, to a large degree, capture the characteristic pattern of the lee-wave that was observed. However, the amplitude of the motion appears to be underestimated by the linear model calculations. This is in agreement with conclusions by other investigators based on comparisons between observations and linear theories in different situations. Our conclusions, based on the present results, appear in section 6.

## 2. Synoptic situation

The Doppler lidar wind data were collected at approximately 1700 UTC (0900 PST), about midway between the synoptic observational times of 1200 UTC on 28 August 1984 and 0000 UTC on 29 August 1984. The mountain peak reaches 4317 m above sea level ($\approx$590 mb) and the flight track is at 3000 m ($\approx$700 mb). The 700 mb and 500 mb charts, displayed in Fig. 2, provide a representative view of the atmospheric conditions that prevailed at the time the data were collected by the aircraft.

At both synoptic times a relatively deep stationary low pressure system was situated over northern Alberta, with a high pressure center just to the east of southern California. Another stationary low pressure system was positioned about 15° to the west of Santa Barbara. The relative positions and steadiness of these systems provided a southwesterly flow from about the 700 to the 100 mb levels, as measured by the soundings taken at Medford, Oregon (Fig. 3). The direction remained steady, but the Medford observations show that the

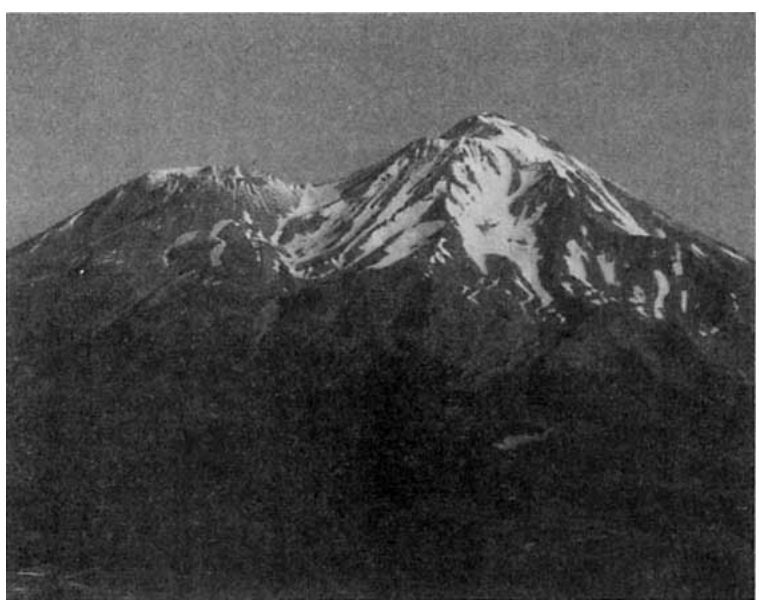

FIG. 1. Photograph of Mount Shasta taken from the Convair 990 aircraft approaching from the south.

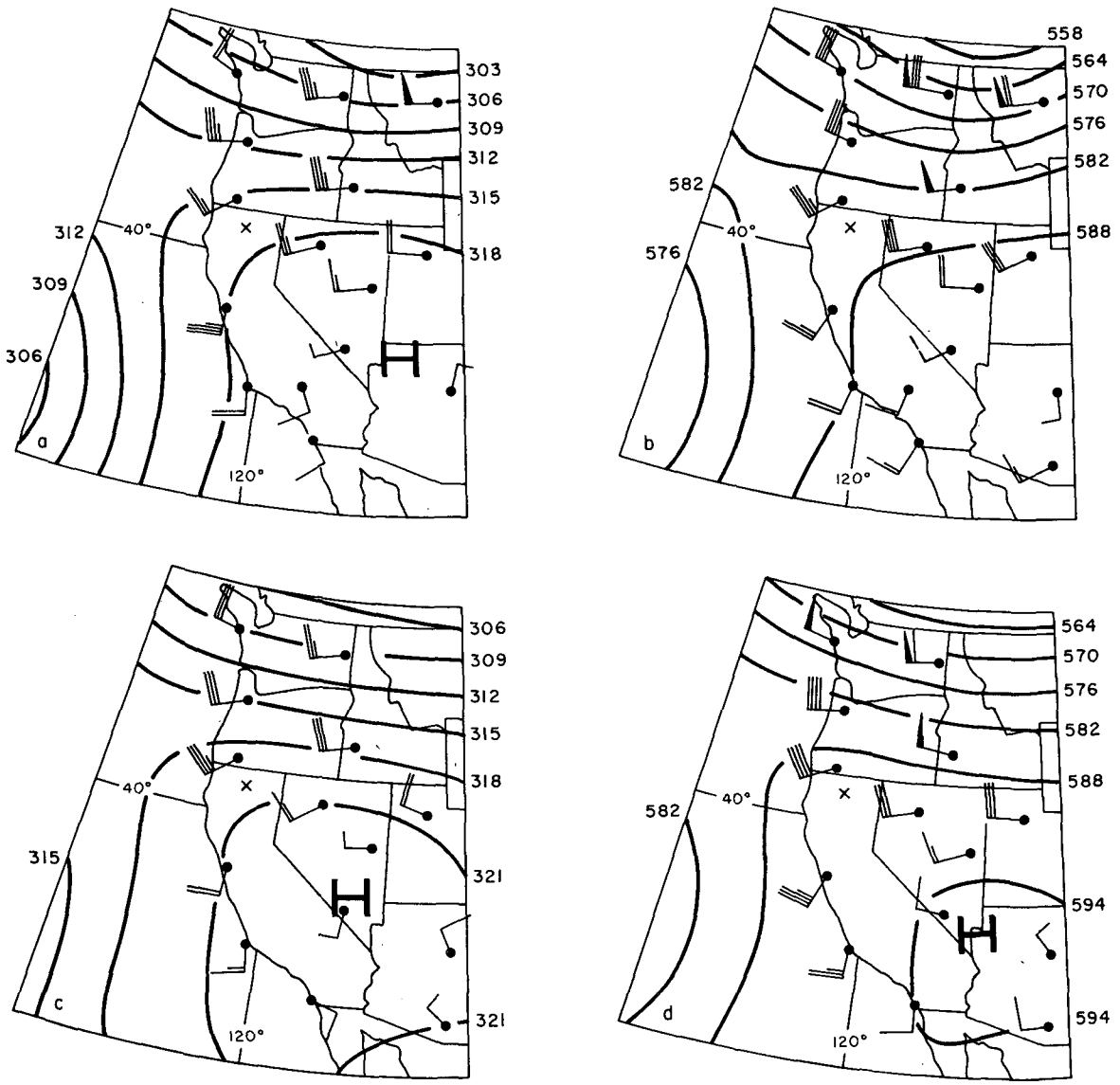


FIG. 2. Upper level synoptic charts. Height contours expressed in decameters, and wind speed in knots. Mount Shasta is located at the position of the *X*, and Medford, Oregon is located immediately to the north. (a) 700 mb at 1200 UTC 28 August 1984; (b) As in (a) except 500 mb; (c) 700 mb at 0000 UTC 29 August 1984; (d) As in (c) except 500 mb.

wind speed at 700 mb increased from 26 to 36 kt while remaining relatively constant at 36–38 kt at 500 mb. Further, the temperature profiles, displayed in the two soundings, exhibit a typical diurnal temperature increase in the late afternoon (0000 UTC), but otherwise little temperature variation is exhibited. The dewpoint temperatures indicate that condensation was not a consideration at flight time. A small globular cap cloud was, in fact, observed over the peak of Shasta during part of the experiment, but otherwise the sky was cloudless.

The available synoptic data support the assumption, used in the model development, that a relatively stationary southwesterly flow existed upstream of Mount Shasta at 1700 UTC 28 August 1984.

## 3. Flight track and environmental parameters

The NASA aircraft circumnavigated Mount Shasta along seven flight tracks during the morning of 28 August 1984. These flight tracks were all between the 3000 and 4200 m levels, but good lidar data were only obtained along one traverse at the 3000 m level. Unfortunately, aerosol contents were low on this day, so signal returns from tracks above 3000 m were inadequate, given the relatively low power of the laser used. In addition electrical malfunctions caused some data dropouts at 3000 m. Doppler lidar wind data were collected along the track between A and B, displayed in Fig. 4. However, onboard sensors did provide temperature, pressure and wind data along each of the seven flight

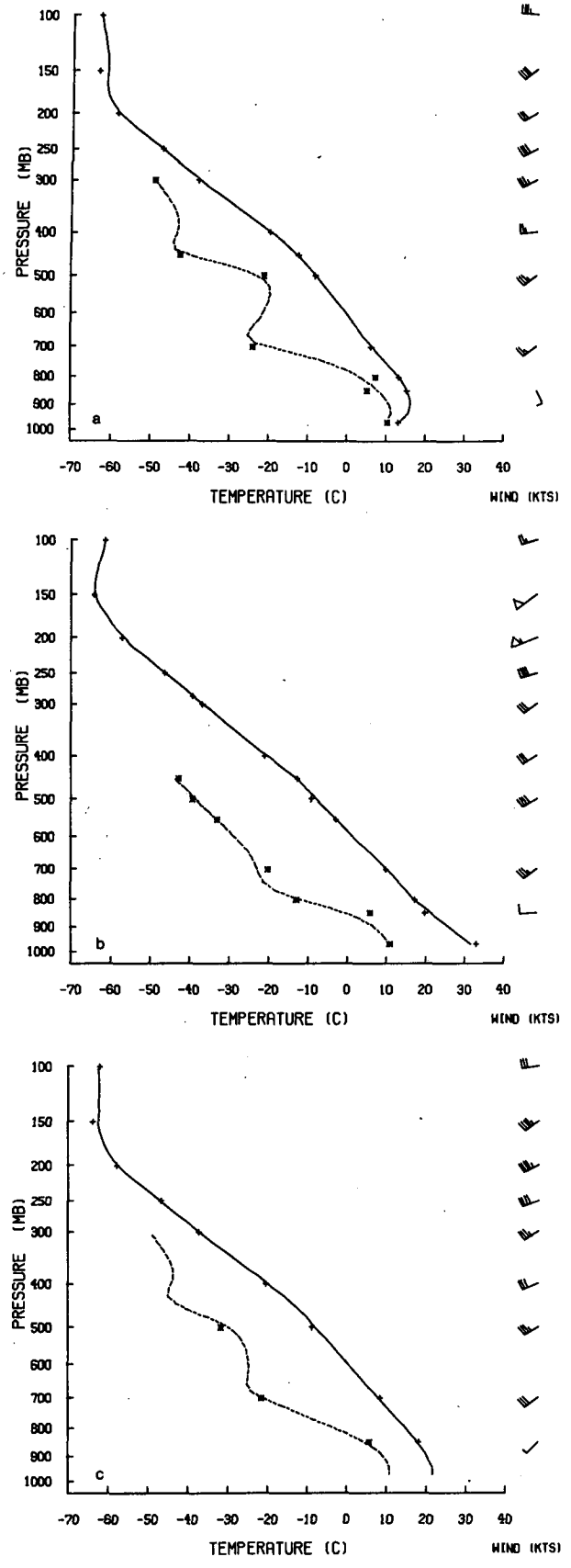


tracks. Consequently, atmospheric properties at the 3000 m level (700 mb) are available from both the aircraft data and the Medford sounding. These properties are provided in Table 1 for comparison.

The Froude number is defined as $\mathrm{Fr} = \bar{u}/Nh_0$, where $\bar{u}$ and $N$ are defined in Table 1 and $h_0$ is the height of the terrain above level ground. The square of this parameter provides a measure of the ratio of the fluid's kinetic energy to the potential energy required to raise a parcel of fluid from level ground to $h_0$. Laboratory experiments by both Brighton (1978) and Baines (1979) indicate that when $\mathrm{Fr} \leqslant 0.5$, fluid below a level $z_c < h_0$ tends to flow around three-dimensional obstacles but the flow is over the obstacle when $z > z_c$. Mount Shasta is characterized by $h_0 \approx 2500$ m. The values obtained from Table 1 yield

$$\mathrm{Fr} \approx 0.5 \text{ (aircraft)},$$

$$\mathrm{Fr} \approx 0.55 \text{ (radiosonde)}.$$

The flow $\bar{u}$ decreases in magnitude below the 3000 m level, but $N$ in the lower layer is relatively constant. This latter feature is evident from the temperature profile in Fig. 3, which exhibits an essentially constant lapse rate between the ground level surrounding Mount Shasta (pressure of about 825 mb) to a level well above the peak. As a consequence, the values of Fr above 3000 m appear to be slightly higher than values typical of the lower atmospheric layer. The indication, based on these computed values, is that all the air may not be able to flow over Mount Shasta. The data to support this supposition is presented in section 4.

The parameter $l_s = N\bar{u}^{-1}$ represents an intrinsic inverse length scale associated with the wave motion maintained by steady stably stratified flow over an obstacle. Evaluation of $l_s$ yields

$$l_s \approx 0.81 \times 10^{-3} \text{ m}^{-1} \text{ (aircraft)},$$

$$l_s \approx 0.72 \times 10^{-3} \text{ m}^{-1} \text{ (radiosonde)}.$$

The flow in the vicinity of the mountain will be affected by its shape. Further downstream the free-wave response, determined by the airstream characteristics, would be evident if the characteristic horizontal mountain scale is comparable with the length scale $\lambda_s = 2\pi/l_s$. The values of $l_s$ above provide an average value of $\lambda_s \approx 8 \times 10^3$ m, and the base radius of Mount Shasta is about $5 \times 10^3$ m. Under this circumstance, Queney (1948) has shown that the waves are dispersive and nonhydrostatic, and that the characteristic vertical

FIG. 3. Medford, Oregon soundings: temperature (solid), dewpoint temperature (dashed) and wind speed expressed in knots. The soundings are reconstructed from standard and significant level data by use of cubic splines as described by Cox (1986). (a) 1200 UTC 28 August 1984; (b) 0000 UTC 29 August 1984; (c) Weighted composite sounding appropriate at 1700 UTC (0900 PST) on 28 August 1984.

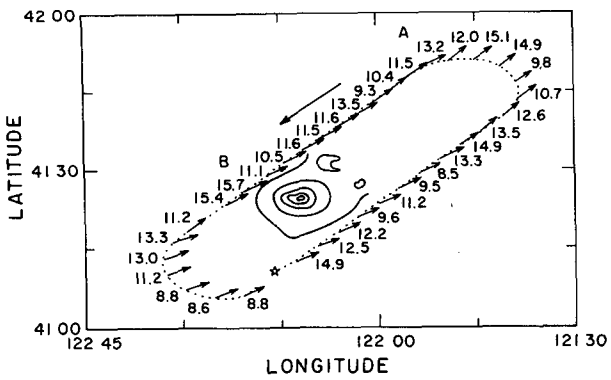


FIG. 4. Flight track at 3000 m. Arrows indicate wind direction, and 300 K should be added to the numbers along the flight track to obtain the potential temperature. The course started at the star, and usable data were obtained between A and B. The innermost topographic contour is 14 000 ft, and the increment is 2000 ft down to 6000 ft.

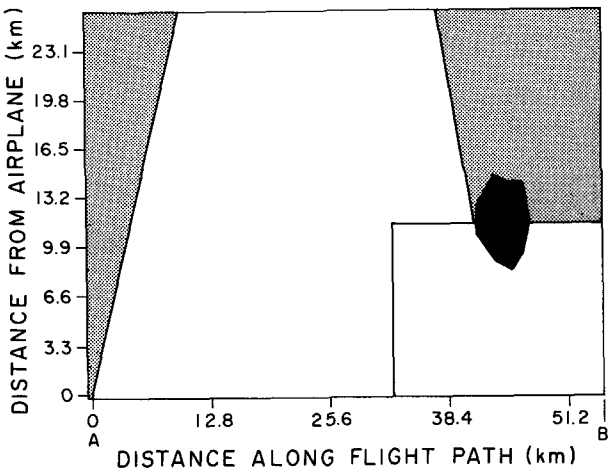


FIG. 5. Region of usable data is confined to the unstippled area. The black area delineates Mount Shasta at the 3000 m level. The small rectangle represents the region where the wind vectors are displayed in Fig. 7.

and horizontal wavelengths are approximately equal with $\lambda \approx \lambda_s$.

## 4. The observed wind field

The aircraft took data for about 5 min along the track shown in Fig. 4. The data boxes, roughly 300 by 400 m in size, are obtained by averaging many returns over a fraction of a second. Even with this averaging, the lack of adequate scatterers leads to a very noisy response at large distances from the aircraft, from which the returns are very weak. However, directly in the lee of the mountain there appeared to be a more abundant set of aerosols, possibly due to slow roll-like overturning that brought particles up from ground level. In this lee region the data were sufficiently noisefree to enable the construction of velocity vectors and horizontal divergence fields.

The construction of the velocity and divergence fields is detailed in the Appendix, and the spatial domain of usable data is illustrated in Fig. 5. Basically, line of sight data from the fore and aft scans are combined to give the vector wind in a slanted sheet. Of course the fore and aft data for a given box are obtained at different times, with the two pieces of data for more distant boxes being as much as a minute apart. Anomalous velocities can appear due to high frequency turbulence that was observed to be present (although there was no gust probe on the Convair 990 to quantify its characteristics).

TABLE 1. Atmospheric properties at the 3000 m level on 28 August 1984. These values correspond to conditions at approximately 1700 UTC.

| | $T$ (K) | $dT/dz$ ($\times 10^{-3}$ K m$^{-1}$) | $\bar{u}^\dagger$ (m s$^{-1}$) | $N^\ddagger$ ($\times 10^{-2}$ s$^{-1}$) |
|---|---|---|---|---|
| Aircraft | 281 | 5.2 | 16.5 | 1.34 |
| Radiosonde | 281.5 | 6.2 | 15.5 | 1.12 |

$^\dagger$ $\bar{u}$ is the total wind speed. The direction coincides with the orientation of the flight track (230 deg).

$^\ddagger$ $N = [g(\gamma_a - \gamma)T^{-1}]^{1/2}$ is the Brunt–Väisälä frequency, where $g = 9.8$ m s$^{-2}$ is the acceleration of gravity, $\gamma_a = 9.8 \times 10^{-3}$ K m$^{-1}$ is the adiabatic lapse rate and $\gamma = -dT/dz$.

The divergence field $D = u_x + v_y$, within a minus two degree (i.e., below the horizontal) sheet is presented in Fig. 6. A smoothing operator is applied (see Appendix) to reduce the high-spatial-frequency noise. It filters on scales shorter than about $10^3$ m, leaving the main features of interest to us which occur on a scale of order $10^4$ m. The main features that are significant are those directly in the lee of the mountain. The instrument cannot handle the short range gates and very bright near-field scattering too close to the aircraft (the bottom of the figure), so that data for perpendicular distances less than about $-7$ are not reliable. Beyond about $+7$, the data are of poor quality because of lack of scatterers.

In the lee there is a significant pool of divergence just behind the mountain. Further downstream there is an elongated pattern of positive divergence which starts at about $x = 10$ and $y = 0$ and goes out to $x = 30$ where the analysis terminates. The onset of this pattern is characterized by a "nose" in the shape of a "vee," and within it there is a wave with a wavelength of about 8 km. This is also seen in the spatial spectrum of the data at $y = 0$ (Fig. 10c). There is a distinct tendency for the positive divergence patterns to tilt downstream with increasing perpendicular distance.

Figure 7 illustrates typical wind vectors (unsmoothed) at flight level (3000 m) near the mountain. In spite of the small-scale variation in the vector field, there is a clearly discernible tendency for the air to turn and flow around the mountain at this level.

We now examine a simple model in order to explain some of these observed features.

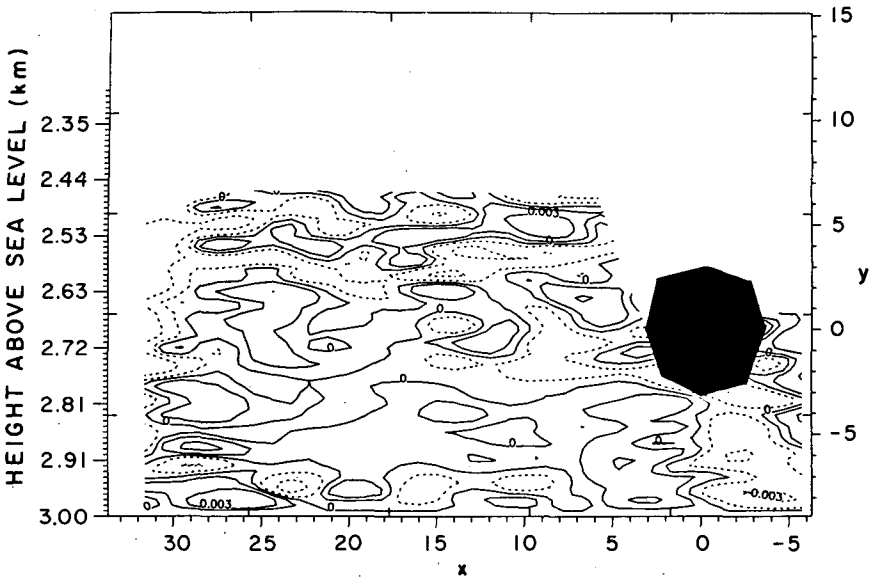


FIG. 6. Divergence field $D$, defined in the text, on a plane tilted two degrees below the 3000 m flight level. The method of data analysis is described in the Appendix. The abscissa (distance downstream) and right ordinate (distance cross-stream) are represented in units of $l_s^{-1} = 1.25 \times 10^3$ m. The elevation of the tilted plane above sea level appears on the left ordinate (km). Dashed contours denote $D < 0$, and $D \geq 0$ are denoted by solid contours. The contour increments are $\pm 10^{-3}$ s$^{-1}$ and $\pm 3 \times 10^{-3}$ s$^{-1}$.

## 5. Model comparison with the observed flow

### a. Linear model

A three-dimensional linear and nonhydrostatic model solution is used for purposes of comparison with the divergence field displayed in Fig. 6. A linear model is not necessarily the best choice in view of the relatively large slope of Mount Shasta, $\partial h/\partial x \sim 0.5$, and the fact that part of the incident southwesterly airstream is diverted around the mountain. This diversion of the air-

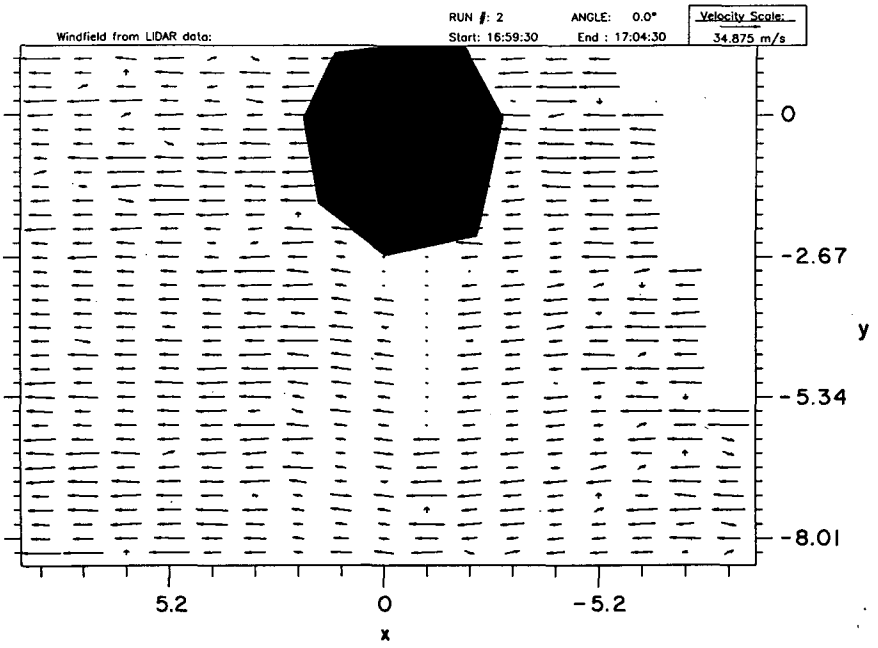


FIG. 7. Velocity vectors at the 3000 m level are displayed in the small rectangle outlined in Fig. 5; the abscissa and the ordinate are represented in units of $l_s^{-1} = 1.25 \times 10^3$ m.

stream is evident in the measured Doppler lidar velocity field at least up to the level of the aircraft (Fig. 7). However, the present purpose is to establish that the lee-side field of observed motions does represent a typical three-dimensional lee-wave pattern. A linear model is adequate for this purpose although, among other limitations, the wave amplitudes would be expected to be underestimated by the linear model, e.g., Smith (1976) and Peltier and Clark (1983).

The nonhydrostatic model is one that has been examined by Sawyer (1962). The equation for the Fourier amplitude of the vertical velocity $W(k_x, k_y; z)$ is given by

$$W'' + \frac{\kappa^2}{k_x^2}\left(\frac{N^2}{\bar{u}^2} - \frac{k^2}{\kappa^2}\frac{\bar{u}''}{\bar{u}} - k_x^2\right)W = 0, \qquad (1)$$

where the Boussinesq approximation is employed; primes denote differentiation with respect to the vertical coordinate $z$; $(k_x, k_y)$ are wavenumbers associated with the downstream and cross-stream coordinates $(x, y)$; and $\kappa^2 = k_x^2 + k_y^2$. The parameter

$$l^2 = \frac{N^2}{\bar{u}^2} - \frac{k_x^2}{\kappa^2}\frac{\bar{u}''}{\bar{u}} \qquad (2)$$

is a function of $z$ since the basic flow $\bar{u}$ and the Brunt–Väisälä frequency $N$ both vary with height. A further restriction imposed on the present model calculation is to assume that $l = l_s = N/\bar{u}$ is constant. This additional model limitation as well as the omission of nonlinearity will be examined later.

The air is assumed to flow over the mountain in vertical planes with the lower kinematic boundary condition being applied at a level surface, not on the finite amplitude mountain itself. Aloft the Eliassen and Palm (1961) radiation condition is applied. These two conditions may be expressed respectively as

$$w(x, y) = \bar{u}\partial h/\partial x, \quad z = 0 \qquad (3)$$

$$\overline{\mathrm{Re}p\ \mathrm{Re}w} > 0, \quad z \to \infty \qquad (4)$$

where $w$ represents the vertical velocity, $h(x, y)$ is the topographic profile of Mount Shasta, $p$ is the perturbation pressure and the bar represents an average over one wavelength $\lambda_x = 2\pi/k_x$. Analytic solutions of (1), with $l = l_s$ and various forms of the topography, have been presented by both Wurtele (1957) and Crapper (1959) among others. The present model solution employs the actual topographic profile in (3). The height contours of Mount Shasta were represented on a grid with approximately a 100 m resolution. The profiles, from two different perspectives, are shown in Fig. 8. The model equation (1) is solved by a discrete Fourier transform approach. The mountain peak resides at the center of a grid representing a swath $10^5$ m by $5 \times 10^4$ m along $(x, y)$. The grid increments are $\Delta = 48.828$ m in each direction, and the summations each extend over 150 wavenumbers $(k_x, k_y)$. Both boundary conditions, (3) and (4), are satisfied and the summations are carried out separately for $k_x > l_s$ and $k_x < l_s$.

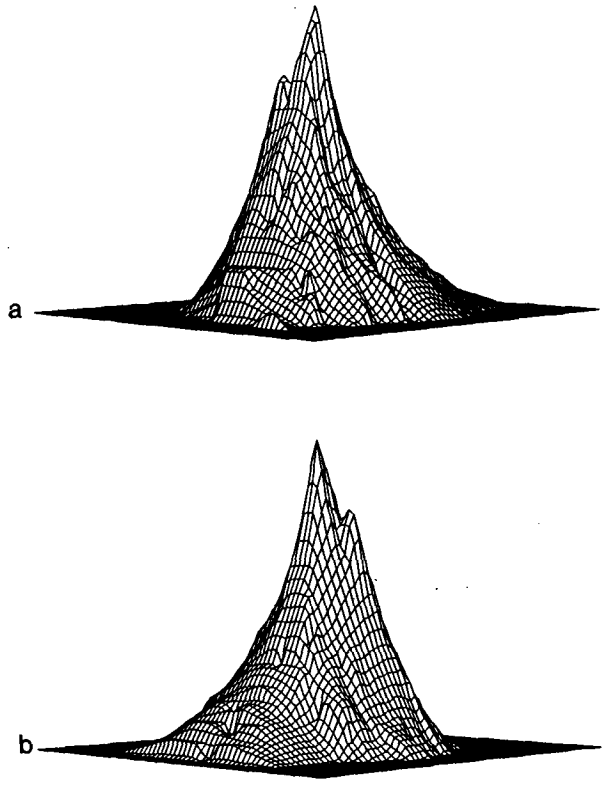


FIG. 8. Mount Shasta from two perspectives. The base is at 5000 ft. (a) facing the mountain from a point on the eastern leg of the flight track in Fig. 4 and (b) facing the mountain from a point on the western leg of the flight track between A and B.

### b. Solution

The solution for the horizontal divergence, $D = u_x + v_y = -w_z$, is displayed on a plane that is tilted two degrees below the flight level, in Fig. 9a. Only about 50 km, in the vicinity of the forcing, of the 100 km computational domain is shown. This solution represents flow over a $2.5 \times 10^3$ m high mountain (base at $1.75 \times 10^3$ m $\approx$ 5800 ft above sea level). The actual base is situated at approximately $1.5 \times 10^3 \approx 5000$ ft above sea level. However, the effective mountain height is possibly different since some low level air flows around rather than over the mountain. Placement of the base at $1.75 \times 10^3$ m provided better agreement with the observed pattern, in Fig. 6, than the linear solutions associated with bases at either higher or lower elevations. The following principal features are characteristic of three-dimensional linear model solutions. The maximum amplitudes appear essentially along the $x$-axis and decay in both the downstream and cross-stream directions: a characteristic wake spreads out with downstream distance. The rapid downstream amplitude decay is associated with the fact that all

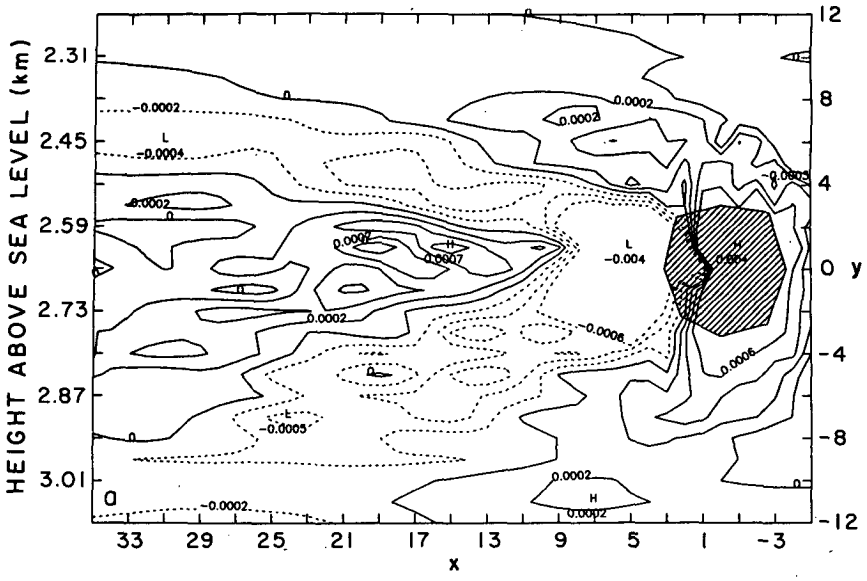


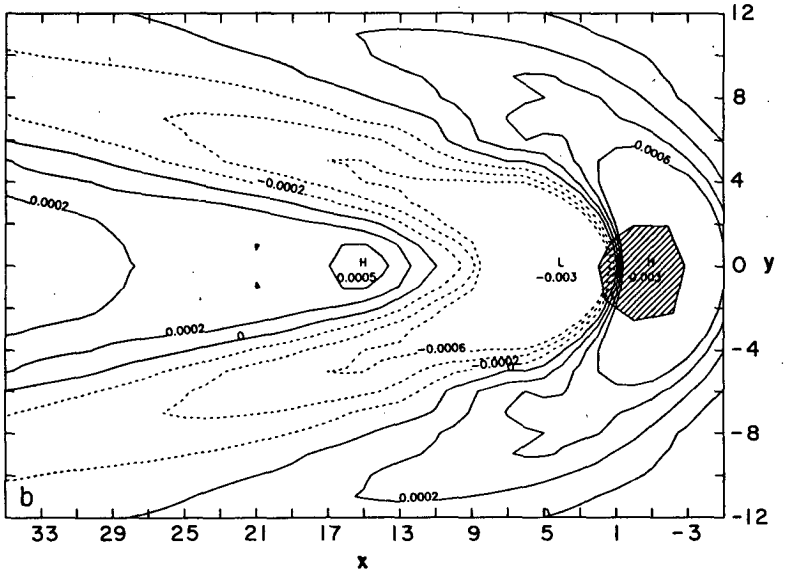


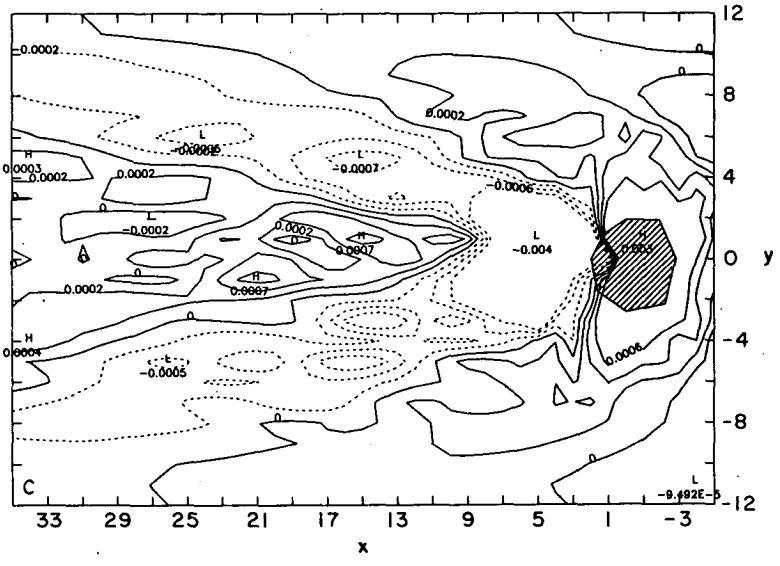

waves transport energy in the vertical direction, and there is no mechanism to confine the waves to the lower troposphere by either partial or total reflection. The lee-wave is not a pronounced feature of the model solution at these elevations, but a wavelength of about $15 \times 10^3$ to $18 \times 10^3$ m is apparent in Fig. 9a.

*c. Comparison with the data*

Both the model solution and the analyzed field of $D$ do exhibit a characteristic feature: the crests of $D$ slope away from the flightpath as one moves downwind in both Figs. 6 and 9a. This is most evident in the characteristic $x - y$ slants in the divergence contours near $y = 0$ and $x = 15$. Two possible mechanisms in this linear model could generate an asymmetry about $y = 0$ in the lee. The upwind slope of the phase surfaces with height $z$, that characterizes the vertical propagation of the stationary wave response, can cause the crests and troughs in the wave pattern within a *sloping* observation surface to be displaced further downstream at lower levels. Alternatively, the complicated and nonsymmetric shape of the mountain itself could be responsible for the predicted asymmetery. Figure 9b shows that the use of an axisymmetric mountain in the calculation, instead of the actual terrain, generates a purely symmetric pattern about $y = 0$ within a horizontal observation surface. However, Fig. 9c shows that within the same surface, for which the vertical phase-tilt effect is entirely absent, the actual mountain generates a lee pattern of $D$ that is almost identical with the pattern in Fig. 9a. Thus, we conclude that the predicted and observed asymmetries are a result of the complex topography of Mt. Shasta.

The downstream wake, which is prominent in Fig. 9a, is less pronounced in the analyzed field of $D$ (Fig. 6). However, there is a clear-cut distinction between the characteristic wave disturbance in the lee, and the relative lack of structure that appears in the motion field close to the aircraft track. This property of the observed field is also in agreement with the expected cross-stream decay of the wave amplitude.

Other comparisons between the solution and the analyzed field $D$ are less satisfactory, and serve to point out the shortcomings of linear modeling of the observed flow. The squared Fourier spectrum of $\partial h/\partial x$, along the $y = 0$ axis, is shown in Fig. 10a. This forcing for the linear problem (3) is dominated by a scale of about 18 km. A secondary peak is at about 6 km. There is also a weak minimum near the characteristic wavelength of the free-wave of 8 km, based on the airstream characteristics at flight level. The downstream squared Fourier spectrum of the model prediction of $D$ at $y = 0$ is shown in Fig. 10b. It reflects the forcing spectrum, with a dominant peak at about 20 km, and a small hump at the free-wave scale. The numerical solution is thus dominated by the direct forcing by a rugged three-dimensional peak.

On the other hand, the downstream squared Fourier spectrum of the data (Fig. 10c) reflects more energy in the free-wave mode at about 8 km than in the directly forced mode at about 17 km. This suggests that the direct mountain forcing is less effective in the real situation. In contrast with the basic assumption of the linear model (3), some of the air must flow around the peak, leading to smaller contribution to the $D$ field at 17 km scales. It is likely that only the uppermost part of Mount Shasta is participating in the generation of the downstream lee waves.

Another notable difference between the $D$ fields is the *difference in sign* of these fields close to the lee slope of the mountain. However, the magnitudes are about the same $D \sim 3$–$4$ ($\times 10^{-3}$ s$^{-1}$). This magnitude corresponds to typical values of $D$ produced by forced flow over Mount Shasta, where the vertical velocity is $w \sim \bar{u}\partial h/\partial x \sim 16$ m s$^{-1} \times 0.5 = 8$ m s$^{-1}$ and $D = -\partial w/\partial z \sim 8$ m s$^{-1} \times (2 \times 10^3$ m$)^{-1} = 4 \times 10^{-3}$ s$^{-1}$. These computations are based on the fact that $w$ vanishes at the ground and that the maximum of $|w|$ is attained near the peak where the slope $|\partial h/\partial x|$ is greatest (see Fig. 8).

At and below the $3 \times 10^3$ m level $\partial w/\partial z < 0$ along and close to the lee slope and observed data confirm that $D$ is primarily positive in this locale (Fig. 6). The relatively large negative values of $w$, associated with flow down the lee slope, are evaluated *at the base of the mountain* in the linear model and $\partial w/\partial z > 0$ above the ground level. This circumstance provides the region of $D < 0$ close to the lee slope in Fig. 9a.

Downstream the divergence field, associated with the observations, exhibits maxima of about $D \sim 1$–$2 \times 10^{-3}$ s$^{-1}$. This value would imply both horizontal and vertical velocity maxima of about 2–4 m s$^{-1}$ since the horizontal and vertical scales are comparable in this apparent nonhydrostatic wave regime. If we take the divergence field in the model solution to be associated with a wavelength about twice that determined in the observed field of motion (see Fig. 10), then the maximum value of $D \sim 5 \times 10^{-4}$ s$^{-1}$ in the model solution corresponds to velocity maxima of about 2 m s$^{-1}$. Similarly the spectral peaks at the 8 km wavelength in Figs. 10b and 10c indicate a ratio of observed to predicted $D$, at this scale, of about 1.7. This ratio between the amplitudes is similar to previous estimates of about 2:1 based on comparisons between observed fields (Smith 1976) and nonlinear model solutions (Peltier and Clark 1983) with linear model solutions.

FIG. 9. Divergence fields from the linear model solution. The ordinates and abscissa are as in Fig. 6. The dashed contours represent $D < 0$, and the solid contours represent $D \geq 0$. The contour increments are $\pm 2 \times 10^{-4}$ s$^{-1}$. In panel a, the observation plane tilts two degrees below the 3000 m level. In panel b there is no tilt, but a smooth axisymmetric bell-shaped mountain centered on $x = 0$ $y = 0$ is used. Panel c is similar to panel b except that the real topography is used.

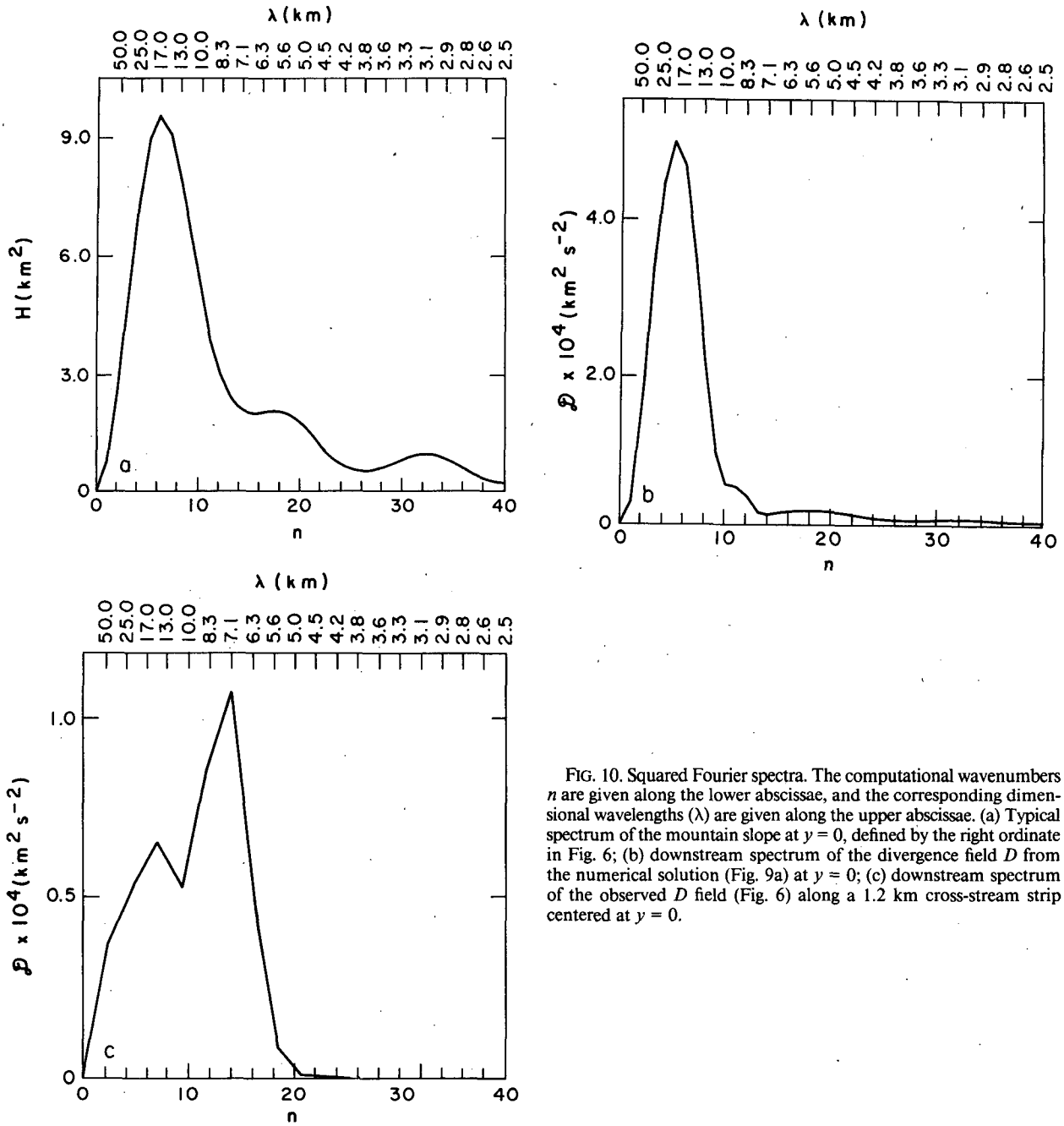


FIG. 10. Squared Fourier spectra. The computational wavenumbers $n$ are given along the lower abscissae, and the corresponding dimensional wavelengths ($\lambda$) are given along the upper abscissae. (a) Typical spectrum of the mountain slope at $y = 0$, defined by the right ordinate in Fig. 6; (b) downstream spectrum of the divergence field $D$ from the numerical solution (Fig. 9a) at $y = 0$; (c) downstream spectrum of the observed $D$ field (Fig. 6) along a 1.2 km cross-stream strip centered at $y = 0$.

Finally, the values of $D$ determined from the data do not appear to decay downstream as rapidly as in the model solution. The observed field may represent a partially trapped wave regime. Figure 11 shows the vertical distribution of $l$, defined by (2). Waves of length $\lambda > 12 \times 10^3$ m propagate vertically at all elevations in the troposphere and stratosphere. However, shorter waves, $\lambda \leqslant 12 \times 10^3$ m, are evanescent in an intervening layer of approximately $5 \times 10^3$ m thickness or greater, and partial reflection of the waves incident from below, would be expected to occur. The relatively slow downstream amplitude decay, in Fig. 6, over approximately two lee-wavelengths could be related to this reflection mechanism. This suggestion could be investigated by carrying out a more realistic model calculation that takes account of both the $z$-variability of the incident flow and the nonlinearity of the wave disturbance.

## 6. Conclusions

Airborne Doppler lidar data obtained in the lee of Mount Shasta are compared with results from a linear

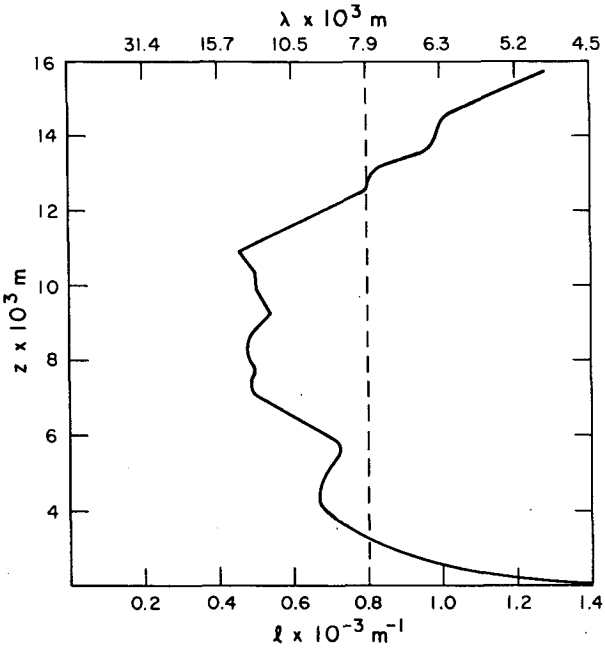


FIG. 11. The parameter $l$ (solid), for $k_x^2/k^2 = \frac{1}{2}$, as a function of height $z$ above sea level, based on the sounding appearing in Fig. 3c. The wavelengths $\lambda = 2\pi/l$ appear above the figure, and $\lambda_s = 2\pi/l_s$ is delineated by the dashed line.

lee-wave model. The model calculation uses the digitized form of Mount Shasta, with a presumed base at 5800 feet. Constant upstream conditions ($\bar{u}$, $N^2$) are assumed and a nonreflective (radiative) upper boundary condition is used.

The model successfully reproduces the observed downstream vee of positive horizontal divergence with imbedded spatially irregular waves. The characteristic predicted and observed wave patterns are consistent, given the approximations in the model. However, the amplitudes of the model downstream divergence is smaller, by a factor of about two, than the observations. We suggest that this is a result of partial reflection of waves from a reflecting layer aloft and nonlinear steepening, processes that both serve to increase the predicted wave amplitudes.

The linear model's most noticeable failing is apparent just to the lee of the mountain, where a strong convergence is generated; whereas divergence dominates in the observed field. This lack of agreement may be associated with the linearization of this very high and steep mountain. The linear calculation is equivalent to a problem where flow is forced by a vertical suction velocity of magnitude $\bar{u}\partial h/\partial x$ coming out of level ground. This placement of the forcing at $z = 0$ in the linearization leads to a leeside divergence that is opposite to that observed, and contrary to what one would expect if the inviscid nonpermeability condition were applied at a finite mountain $h(x, y)$ sticking high up into the fluid.

This experiment has demonstrated the potential for the airborne Doppler lidar in studying stratified airflow around isolated topography. Ideally a more extensive dataset, particularly observations on lower flight tracks (which are somewhat difficult to orchestrate, given the terrain and the size of the aircraft), could be used in conjunction with a nonlinear model to provide more physical insights than presented here. Mount Shasta is located well away from any manmade sources of aerosols, and on stably stratified days low-level aerosols are not readily mixed up to altitudes corresponding to the mountain top. Possible future modifications to the instrument that would increase its transmitting power might permit some very elegant field observations of airflow over and around large isolated topography. The ability to obtain a rather complete three-dimensional wind field in about an hour would provide an opportunity to study such phenomena as the location of the dividing streamline, horseshoe vortices, and trailing longitudinal vortices, as observed, for example, in Brighton's (1978) laboratory experiments.

*Acknowledgments.* We would especially like to thank Dan Fitzjarrald of the Marshall Space Flight Center for helping to organize and carry out the research flight. We are also grateful to Jeff Rothermel, of the same organization, who helped with the initial data processing. Patrick Callaghan at the University of Colorado provided able assistance in writing the data analysis routines and producing computer output from the linear model, and Craig Hartsough provided Fig. 3. Support for this investigation was provided by The Universities Space Research Association through Contract NAS8-35919 with the National Aeronautics and Space Administration.

## APPENDIX

### Data and Method of Analysis

Data in a rectangle, approximately 25 km by 50 km, were available for analysis. The region is shown in Fig. 5. Vector winds displayed in Fig. 7 are contained within the smaller rectangle near the mountain. These data were collected over about a five minute period as the plane moved from A to B (see also Fig. 4).

The data are comprised of winds along the line of sight from a forward scan (f) and an aft scan (a) by the Doppler lidar wind system. A schematic, displaying the line of sight wind vectors, and their relation to the actual wind vector is provided in Fig. 12a.

This schematic isolates the technique used to compute wind vectors **v**. The forward scan at time $t_1$ intersects the aft scan at time $t_2 = t_1 + \Delta t$. The airspeed is $c \approx 170$ m s$^{-1}$ and the total distance normal to the aircraft, over which data are available, is $\Delta y \leqslant 25 \times 10^3$ m. The viewing angle is $\phi = 20$ deg. Consequently, the maximum distance between $t_1$ and $t_2$ is $\Delta x \approx 18 \times 10^3$

m, so that $\Delta t \leqslant 100$ s since the observed motions are relatively stationary, relative to the mountain, it may be assumed that the wind vectors do not change over time $\Delta t$.

The relationship between the wind speeds are

$$\left.\begin{aligned} |\mathbf{v}_f| &= |\mathbf{v}| \sin(\phi + \psi) \\ |\mathbf{v}_a| &= |\mathbf{v}| \sin(\phi + \psi) \end{aligned}\right\}, \tag{A1}$$

where $|\mathbf{v}|$ and $\psi$ are to be determined. The angle $\psi$ is determined by

$$\left.\begin{aligned} \cos\psi &= \frac{1}{2\sin\phi}\,\frac{|\mathbf{v}_f| + |\mathbf{v}_a|}{|v|} = \frac{u}{|\mathbf{v}|} \\ \sin\psi &= \frac{1}{2\cos\phi}\,\frac{|\mathbf{v}_f| - |\mathbf{v}_a|}{|v|} = \frac{v}{|\mathbf{v}|} \end{aligned}\right\} \tag{A2}$$

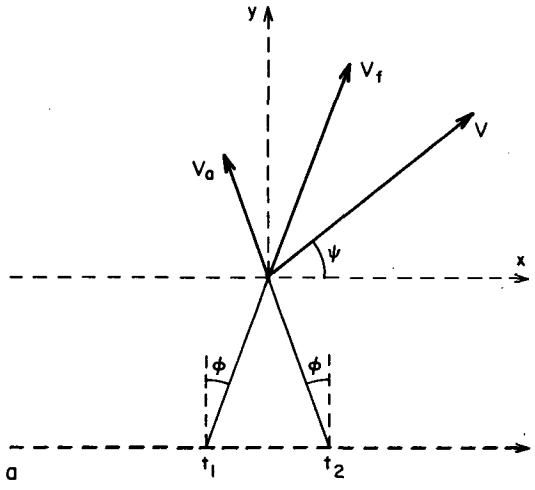


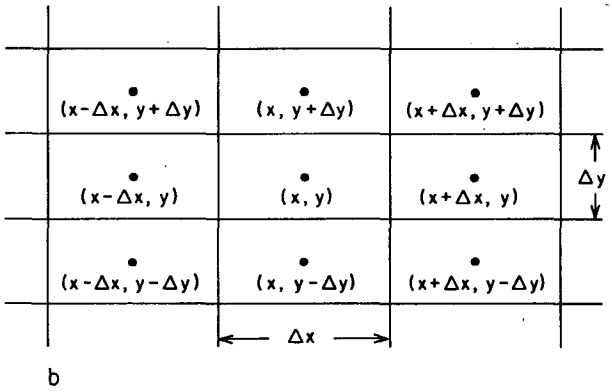


FIG. 12. (a) Schematic showing the line of sight vector wind measurements $\mathbf{v}_a$ and $\mathbf{v}_f$. $\mathbf{v}$ is the vector wind determined as described in the Appendix. The angle $\phi$ is 20 degrees; $(t_1, t_2)$ indicate the times when the aircraft is at the indicated positions. (b) Schematic of the grid used for the calculation of the divergence $D$ (not drawn to scale).

where $\mathbf{v} = u\mathbf{i} + v\mathbf{j}$. The $(x, y)$ velocity components $(u, v)$ may be determined from (A2) and the velocity vectors $\mathbf{v}$ displayed, as in Fig. 7. These vectors represent the average velocity in a box $(\Delta x, \Delta y) = (1.28, 0.33) \times 10^3$ m.

The horizontal divergence is determined from the relation

$$\frac{\partial u}{\partial x} + \frac{\partial v}{\partial y} \approx \frac{(u + \bar{u})_{x+\Delta x,y} - (u + \bar{u})_{x-\Delta x,y}}{4\Delta x} + \frac{(v + \bar{v})_{x,y+\Delta y} - (v + \bar{v})_{x,y-\Delta y}}{4\Delta y}, \tag{A3}$$

where

$$\left.\begin{aligned} \bar{u}|_{x+\Delta x,y} &= \frac{u|_{x+\Delta x,y+\Delta y} + u|_{x+\Delta x,y-\Delta y}}{2} \\ \bar{u}|_{x-\Delta x,y} &= \frac{u|_{x-\Delta x,y+\Delta y} + u|_{x-\Delta x,y-\Delta y}}{2} \\ \bar{v}|_{x,y+\Delta y} &= \frac{v|_{x+\Delta x,y+\Delta y} + v|_{x-\Delta x,y+\Delta y}}{2} \\ \bar{v}|_{x,y-\Delta y} &= \frac{v|_{x+\Delta x,y-\Delta y} + v|_{x-\Delta x,y-\Delta y}}{2} \end{aligned}\right\}. \tag{A4}$$

The relative positions of the components $(u, v)$ are shown in Fig. 12b. The horizontal divergence is calculated at the point $(x, y)$ for each box in the total field, displayed in Fig. 6, by using data in the eight surrounding boxes to evaluate (A3). A *smoothed divergence field* is determined by taking the unweighted average value of the divergences in each of the nine boxes, and associating this average value with the point $(x, y)$. Repetition provides a *second smoothed divergence field.* The latter field is the one shown in Fig. 6. The small-scale detail has been eliminated, to a large extent, leaving a field which has a structure similar to the one displayed by the unsmoothed model solution.

## REFERENCES

Baines, P. G., 1979: Observations of stratified flow past three-dimensional barriers. *J. Geophys. Res.*, **84,** 7834–7838.

Bilbro, J., G. Fichtl, D. Fitzjarrald, M. Krause and R. Lee, 1984: Airborne Doppler lidar wind field measurements. *Bull. Amer. Meteor. Soc.*, **65,** 348–360.

Bluestein, H. B., R. J. Doviak, M. D. Eilts, E. W. McCaul, R. Rabin, A. Sundra-Rajan and D. S. Zrnic', 1986: Analysis of airborne Doppler lidar, Doppler radar, and tall tower measurements of atmospheric flows in quiescent and stormy weather. NASA Contractor Rep. 3960, George C. Marshall Space Flight Center, 165 pp.

Brighton, P. W. M., 1978: Strongly stratified flow past three-dimensional obstacles. *Quart. J. Roy. Meteor. Soc.*, **104,** 289–307.

Clark, T. L., and R. Gall, 1982: Three-dimensional numerical model simulations of airflow over mountainous terrain: A comparison with observations. *Mon. Wea. Rev.*, **110,** 766–791.

Cook, N. J., and B. H. Coulson, 1977/78: Wind conditions around the Rock of Gibraltar. *J. Ind. Aerodyn.*, **2,** 289–309.

Cox, K. W., 1986: Analysis of the Pyrenees lee wave event of 23 March 1982. *Mon. Wea. Rev.*, **114,** 1146–1166.

Crapper, G. D., 1959: A three-dimensional solution for waves in the lee of mountains. *J. Fluid Mech.*, **6,** 51–76.

Eliassen, A., and E. Palm, 1961: On the transfer of energy in stationary mountain waves. *Geofys. Publ.*, **22,** 1–23.

McCaul, E. W. Jr., H. B. Bluestein and R. J. Doviak, 1986: Airborne Doppler lidar techniques for observing severe thunderstorms. *Appl. Opt.*, **25,** 698–708.

Peltier, W. R., and T. L. Clark, 1983: Nonlinear mountain waves in two and three spatial dimensions. *Quart. J. Roy. Meteor. Soc.*, **109,** 527–548.

Pickersgill, A. O., and G. E. Hunt, 1981: An examination of the formation of linear lee waves generated by giant Martian volcanoes. *J. Atmos. Sci.*, **38,** 40–51.

Queney, P., 1948: The problem of airflow over mountains: A summary of theoretical studies. *Bull. Amer. Meteor. Soc.*, **29,** 16–26.

Sawyer, J. S., 1962: Gravity waves in the atmosphere as a three-dimensional problem. *Quart. J. Roy. Meteor. Soc.*, **88,** 412–425.

Smith, R. B., 1976: The generation of lee waves by the Blue Ridge. *J. Atmos. Sci.*, **33,** 507–519.

Walter, B. A. Jr., and J. E. Overland, 1982: Response of stratified flow in the lee of the Olympic Mountains. *Mon. Wea. Rev.*, **110,** 1458–1473.

Wurtele, M. G., 1957: The three-dimensional lee wave. *Beitr. Phys. Freien Atmos.*, **29,** 242–252.